

# Fabrication of a Fabry–Pérot Cavity in a Microfluidic Channel Using Thermocompressive Gold Bonding of Glass Substrates

Hua Shao, *Student Member, IEEE*, Dhiraj Kumar, *Student Member, IEEE*, Stewart A. Feld, *Member, IEEE*, and Kevin L. Lear, *Member, IEEE*

**Abstract**—This paper presents a simple, low-cost, and reliable process for the fabrication of a microfluidic Fabry–Pérot cavity in a Pyrex glass substrate. The microfluidic channels were etched in HF solution on a glass substrate using a Cr/Au/photoresist etching mask resulting in a channel bottom roughness of 1.309 nm. An effective thermocompressive gold–gold bonding technique was used to bond the photolithographically etched glass substrates inside a 350 °C oven in a  $10^{-3}$  torr vacuum. Pressure was applied to the glass pieces by using two aluminum blocks with intermediate copper sheets. This method takes advantage of using Cr/Au layers both as a wet etching mask and as intermediate bonding layers, requiring only one lithography step for the entire process. The fabrication method is also compatible with the incorporation of dielectric mirror coatings in the channels to form a high-finesse Fabry–Pérot cavity. A parallelism of 0.095 degrees was measured, and a finesse as high as 30 was obtained using an LED. The microfluidic cavity developed here can be used in electrophoresis and intracavity spectroscopy experiments. [1375]

**Index Terms**—Fabry–Pérot cavity, finesse, gold thermocompressive bonding, microfluidics.

## I. INTRODUCTION

VARIOUS microelectromechanical system (MEMS) based lab-on-a-chip analytical systems have been recently developed for the analysis of biological samples such as proteins, cells, and DNA. Among the various detection techniques, optical methods are of great interest due to their large information capacity, flexibility, and compatibility with present semiconductor processing techniques. Microfluidic Fabry–Pérot (FP) cavities are being developed for a wide range of applications, including microsphere spectroscopy [1], biocavity lasers [2], microcavity fluidic dye lasers [3], and optical FP filters [4]. For all these applications, the system performance is highly dependent on device fabrication techniques. Considerable attention is now directed toward simplifying and improving the reliability of the manufacturing steps.

Glass-based microfluidic devices, especially those coated with reflective thin films inside the etched channels, are very

attractive for microcavity spectroscopy. Detection of microstructures within the cavity is based on the optical resonant frequencies of the fluidic cavity, which are determined by the cavity geometry. Therefore, cavity stability is a major factor in the system performance. Compared to polydimethylsiloxane (PDMS), glass offers better rigidity and easier control of surface properties, which make it desirable for applications that require robust and stable surface characteristics. Wafer bonding is a critical step in the fabrication of microfluidic devices and should not reduce the chemical inertness, uniformity, or integrity of the etched channels. However, most of the currently developed FP microfluidic cavities use either a microbridge without wafer bonding [1], [2] or are sealed with photoresist [3], [4] or photodefinable epoxy [5]. Controlling the cavity length and the parallelism between the superstrate and substrate requires strong bonding. This paper reports an effective and reliable way to make sealed, microfluidic, FP cavities in a glass substrate that are suitable for electrophoresis and intracavity spectroscopy experiments.

In the work reported here, microchannels were wet etched into glass substrates using a standard photolithographic process. Two patterned glass wafers were then sealed using a thermocompressive gold–gold diffusion bonding technique. This method has several advantages over present microfluidic FP cavity fabrication methods in manufacturing complexity, surface smoothness, cavity rigidity, and bonding temperature. First of all, it makes use of the etching mask as intermediate bonding layers, which greatly simplifies the fabrication process by eliminating complicated and strict wafer cleaning processes. Second, using gold as a bonding layer is compatible with dielectric or other metallic mirror coatings to be incorporated in the channels to make high finesse FP cavities as long as the coatings are limited to the channel bottoms. For example, while gold provides high reflectivity in the near-infrared, silver or aluminum would be more suitable in the visible range, and dielectric coatings could provide low loss reflectors across the spectrum. Furthermore, the bonding temperature of 350 °C for the present paper is much lower than for glass-to-glass direct wafer bonding, which requires a bonding temperature of 580 °C for soda-lime glass [6], or 500 °C to 650 °C [7]–[9] for borosilicate glass. Finally, the surface property of the etched channel is much easier to control than with PDMS. The gold coating and sealing layer can be further patterned to facilitate

Manuscript received July 6, 2004; revised November 15, 2004. This work was supported by DARPA under Research Contract E-21-F89-G1. Subject Editor H. Zappe.

The authors are with Electrical and Computer Engineering Department, Colorado State University, Fort Collins, CO 80523 USA (e-mail: lshao@engr.colostate.edu; klllear@engr.colostate.edu).

Digital Object Identifier 10.1109/JMEMS.2005.845447

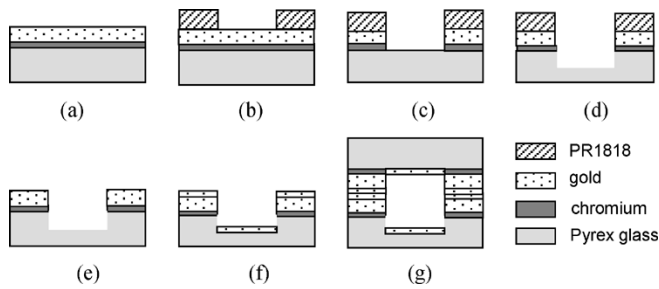


Fig. 1. Schematic diagram of the device fabrication process. (a) Cr/Au evaporation. (b) Photolithography. (c) Cr/Au wet etching. (d) Glass wet etching. (e) Photoresist removal. (f) Mirror coating. (g) Wafer bonding.

the integration of metallic electrodes, which will make it suitable for electrophoresis experiments.

## II. DEVICE FABRICATION

### A. Channel Definition and Mirror Formation

Fabrication of thermocompressively bonded, microfluidic FP cavities began by wet-etching channels into glass substrates using a Cr/Au/photoresist mask as illustrated with cross-sectional diagrams in Fig. 1(a)–(g). Pyrex 7740 borosilicate glass slides ( $1'' \times 1.5'' \times 0.7$  mm) were used to form the microfluidic channels due to their advantages over other materials, such as robustness, high resistance to chemicals, a wide optical transmission range, and high electrical insulation. The glass substrates were first cleaned with acetone, methanol, and deionized (DI) water prior to the deposition of etch masking layers. A thin, 30-nm, Cr layer followed by a 120-nm gold layer were e-beam evaporated on the glass substrate. The Cr layer was included to increase the adhesion between the gold film and the glass substrate. Shipley PR1818 photoresist was spun on the Cr/Au coated glass substrate at 4000 rpm and UV exposed with an energy density of  $15 \text{ mJ/cm}^2$  for 11 s. The mask used for the photoresist exposure was a high resolution (1500 dpi) laser printed transparency designed with a computer illustration program and containing patterns for channel widths of 50 to  $280 \mu\text{m}$ . The exposed, positive tone photoresist over the channels was removed with AZ400K developer for 45 s. The underlying gold was then etched in commercial etchant consisting of potassium iodide and a mixture of cerium nitrate. Subsequently, the Cr over the channel was etched with nitric acid. Leaving the patterned photoresist as a protective layer for the gold mask, the whole wafer was dipped into 49% HF at room temperature for 2 min. A channel depth of  $15 \mu\text{m}$  was obtained, as measured by a surface profilometer. The observed channel edges are curved due to the undercut of the metal mask during the wet etching step. Consequently, the actual channel width is larger than the designed value by  $30 \mu\text{m}$  as a result of the isotropic etching of glass by the HF solution [10]. Narrow channels with large aspect ratios could be fabricated without undercut by using dry etching followed by an optional, brief wet etch if necessary to improve the roughness of the etched channel. For completely dry etching, the minimum channel width would be determined by lithographic constraints and the anisotropy of the etch.

High-quality mirror coatings are critical to the proper function of the Fabry–Pérot cavity. In order to remove the particles left inside the etched channels in the photoresist developing process, a 30-s reactive ion etch was performed before the mirror coating. Wet rather than dry etching was primarily used in these experiments to enhance the smoothness of the etched channel. In the simple, unmasked process a thin, 35-nm gold mirror layer was electron beam evaporated on the entire sample after stripping the photoresist. Alternative processes for coatings other than gold are discussed later.

Surface roughness of the etched channel was studied by Atomic Force Microscopy (AFM) since roughness affects the optical reflectivity of the mirror coatings, which imposes an upper limit on finesse. Fig. 2 shows the AFM images taken from the bottom of the etched channel. The measurements indicated a rms roughness of 1.309 and 1.765 nm before and after the gold coating, respectively. This surface roughness meets the requirements for optical mirrors, which can be utilized in the intracavity spectroscopy experiments. The detrimental optical effects of various types of mirror defects have been extensively studied [11]–[13]. In this paper, the allowed maximum finesse was calculated using the closed form formula in [12],  $F_{total} = (F_{ideal}^{-2} + F_d^{-2})^{-1/2}$ , where  $F_d$  is the surface roughness limit on finesse defined as  $F_d = \lambda / (2\sqrt{3}\sigma)$  with  $\sigma$  designating the rms surface roughness and  $\lambda$  being the optical wavelength. From this expression, the rms surface roughness of 1.765 nm allows a maximum cavity finesse of 145.56. The ideal finesse of the cavity is 43.3 based on the 93% reflectivity of the 35-nm gold mirrors at 890 nm. The resultant total finesse including surface roughness is  $F_{total} = 41.48$ . The increased rms roughness after coating may be caused by small clusters or other defects in the gold layer resulting from the relatively high 0.3–0.4 nm/s deposition rate. Further improvement of the surface roughness can be expected by decreasing the concentration of the HF solution in the wet etching process [14]. A multilayer Cr/Au mask should be used for channel depths larger than  $50 \mu\text{m}$  in order to prevent pinholes in the masked area [15].

Dielectric or a variety of metallic mirror coatings, such as aluminum or silver, can also be deposited in the channel without interfering with the gold surfaces for bonding, by slightly modifying the fabrication steps. In this case, the steps through channel etching would be carried out as described earlier, but the etch masking photoresist would be left in place while the mirror coating is deposited in the exposed channel. The photoresist can then be used to lift off the mirror coating material outside the channel, leaving the underlying gold exposed for subsequent bonding. The mirror deposition temperature must be kept below the photoresist reflow temperature to allow optimum lift off. In the design process developed in this work, only the etched channel portions are optically transparent or selectively coated with thin-film mirrors so that light will be blocked outside the channel region.

Another, unetched, Pyrex glass sample was prepared for the superstrate at the same time as the substrate containing the etched channel. The superstrate was fabricated in a nearly identical process as that used for the substrate including etching of the metal layers in the channel region, but without etching

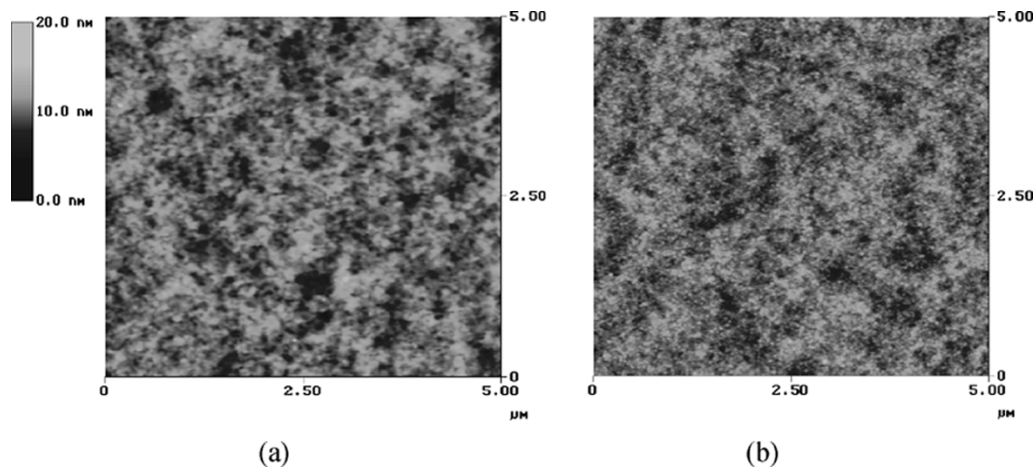


Fig. 2. (a) AFM image of a 15  $\mu\text{m}$  deep etched Pyrex glass channel surface before gold coating. The rms roughness is 1.309 nm. (b) AFM image of an etched channel surface, with a RMS roughness of 1.765 nm, after evaporating a layer of 35-nm gold at a 0.4 nm/s evaporation rate.

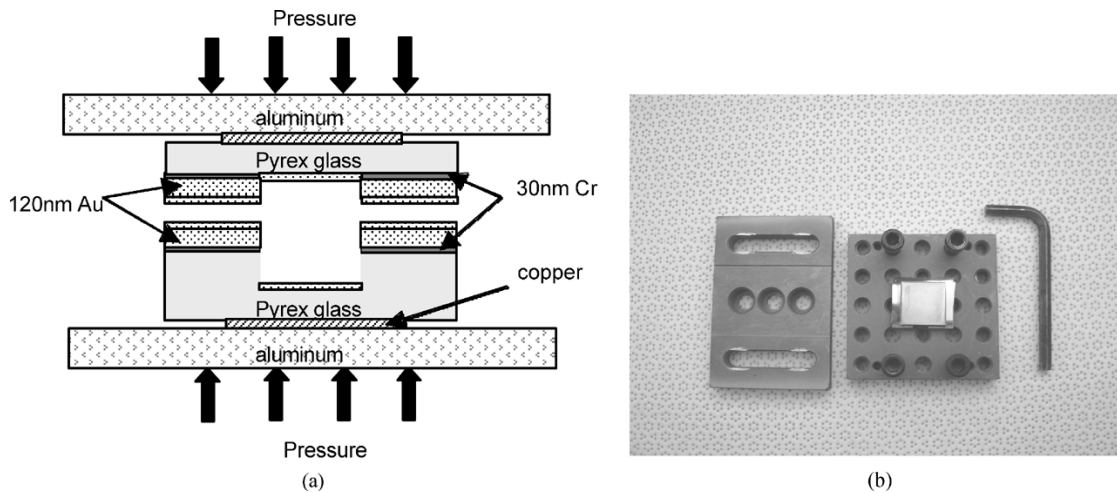


Fig. 3. (a) Schematic diagram of thermal compressive gold-gold diffusion bonding. (b) Plates that were used to apply pressure to the glass substrates.

the glass layer. The thin gold mirror layer was evaporated on the superstrate at the same time as the substrate in order to keep the substrate and superstrate mirror layer thicknesses and thus optical reflectivities matched as this provides a higher finesse FP cavity.

### B. Thermocompressive Gold-Gold Diffusion Bonding

The patterned glass substrate and superstrate with gold coatings were bonded together using the thermocompressive gold-gold diffusion bonding technique [16]. The schematic diagram in Fig. 3(a) shows the bonding of the glass substrate and superstrate including Au mirror coatings in the channel. Strong bonding was obtained by applying pressure to the glass samples by clamping them between aluminum plates shown in Fig. 3(b). Four bolts at the corners of the plates were tightened using an Allen wrench to apply a torque of approximately 130 lbs in. Prior to the final clamping the superstrate and substrate were aligned under a microscope system with the help of alignment marks visible through open holes in the plates.

Shearing tests and subsequent failure analysis showed that bonding occurred primarily at the outer edges of the sample using the apparatus just discussed. This is attributed to the bolt

placement at the corners of the plate causing minute bowing in the plates and thus greater pressure near the edges of the sample. In order to deliver force more uniformly to the central part of the glass substrates, two small (1.85 cm  $\times$  1.85 cm  $\times$  0.142 cm) polished copper sheets were inserted between both glass and aluminum interfaces. Other researchers have suggested the use of temporary flat metal plates in the initial bonding process for thermocompressive glass wafer bonding [17]. The high thermal conductance of copper, 4 times higher than that of the aluminum, promotes more uniform heat distribution across the glass samples as well. An initial bonding process without inserting the copper plates needs to be performed if the patterns on the glass substrate and superstrate need to be aligned by seeing through the clamps. The clamped assembly of the glass samples, copper sheets, and aluminum plates was then put into an oven evacuated to a pressure of about  $10^{-3}$  torr. The sample temperature was gradually increased over 4 h to a final temperature of 310–350  $^{\circ}\text{C}$ , which was held for 20 min before cooling the samples for 2 h. Strong and homogenous bonding was achieved using this method. The impact of the bonding temperature on the strength of the bonded interface is discussed in the next section.

TABLE I  
SHEAR TEST OF THERMAL COMPRESSIVE BONDING STRENGTH

Wafer bonding temperature	Shear force ( <i>Newton / cm<sup>2</sup></i> )	Observed failure mode
310°C	3.833	Chromium separates from the glass
330°C	5.767	Gold layers separate
350°C	13.557	Glass fractures

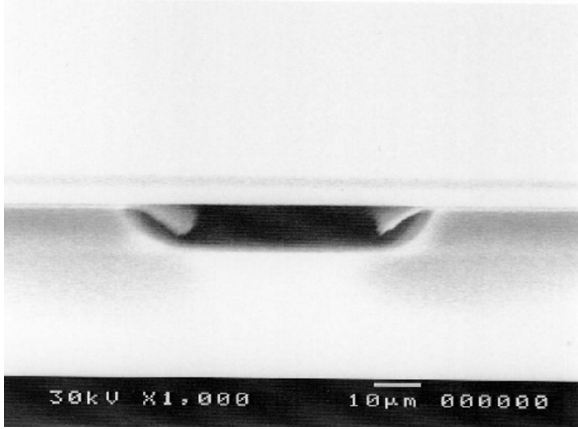


Fig. 4. SEM picture of a cavity cross section after thermocompressive bonding. Ordinary glass coverslips were used for making this cavity to simplify cutting the bonded sample in cross section.

### III. EXPERIMENTS

Accurate control of the FP cavity length and thus transmission spectrum requires uniform bonding of the substrate and superstrate without an intervening gap that can vary in size. In this paper, bonding strength has been used to quantify the quality and completeness of bonding. In order to test the bonding strength, shear tests were performed on three (2 cm × 3 cm) samples bonded at 310 °C, 330 °C, and 350 °C. Table I lists the shear force per bonded area required to separate the substrate and superstrate as well as the observed failure modes. The observed failure location of the samples indicates that the bonding happens mostly on the outer edges of the wafer at temperatures lower than 350 °C. Strong bonding across the entire sample occurs around 350 °C, which significantly increases the shear force.

A scanning electron microscope image of the sealed channel resulting from the 350 °C thermocompressive bonding process is shown in Fig. 4. The image shows there are no gaps between the metal films in the regions outside the channel. Undercut metal layers are apparent at the edges of the channel. Typical of gold thermocompressive bonding [16] is that the combination of heating and clamping pressure in the vacuum causes atoms to diffuse and mix between the gold layers on the two glass slides, forming a single gold layer that bonds the two parts together. The diffusion process requires clean surfaces to allow intimate contact between the gold layers.

The channel layout can also impact the quality of the bonding. Large unetched areas should be provided between channel regions to ensure successful bonding. Designs with channels extending to the sample edge allow trapped air to readily escape from the bonded cavity. The gold bonded glass technique presented here does allow greater flexibility in channel layout than

some other methods. For example, cavities sealed with photo-sensitive epoxy require a critical bonding temperature to prevent a clog within the channel while still maintaining a strong bonding strength [5].

Optical measurements of the microfluidic cavity are useful for verifying the quality of the bonding without resorting to destructive tests required for cross sectioning. The cavity depth after bonding can be extracted from the transmission spectra based on the wavelength position and spacing of the optical microcavity modes. Fig. 5 shows the optical transmission spectra of the FP microfluidic cavity when flood exposed by a broadband microscope white light from the superstrate side while a 62.5 μm core diameter multimode optical fiber was used to collect the transmitted light on the opposite side. The figure shows spectra for both an air filled and water filled channel. The shift in the spectrum corresponds to an increased optical thickness due to the refractive index of water. The broadband microscope white light excites several longitudinal modes in the transmission spectra, which makes the cavity depth measurement more accurate by fitting a large number of modes with the theoretical simulations. TFCalc, a thin-film design software package, was used to simulate the cavity transmission spectrum for the air filled cavity with the results presented in Fig. 5. A cavity length of 14.828 μm predicted by fitting the simulation result to the experimental spectra corresponds very well with the etching depth of 15 μm measured by the surface profiler. The good correspondence between the measured etch depth and the measured depth of the bonded cavity indicates the accurate cavity length control that is available using the method presented in this paper. Other methods may have greater variation between the designed and measured cavity lengths. For example, an uncertainty of 1 μm in the thickness of the bonding layer of a 15 μm deep microfluidic dye laser cavity, formed and bonded using the SU-8 photoresist, was previously reported [18].

The measured finesse using the broadband microscope light is much lower than corresponding simulations in Fig. 5 due to the imperfect collimation of the extended source. A customized microscope system, shown in Fig. 6, was used to analyze the transmission spectra of the microfluidic cavity illuminated by LEDs from the bottom side. The fiber coupled Ocean Optic Spectrometer (HR2000), with a 0.3-nm resolution and a spectral response range of 865–1020 nm, collects the transmitted light. An improved finesse over a narrow-band obtained by using a well-collimated high power LED (Hamamatsu L2690-02) is shown in Fig. 7. Although the LED has a narrower wavelength range than the microscope light, leading to fewer excited longitudinal modes of the cavity, it results in higher finesse. A biconvex lens ( $f = 30$  mm) collimated the LED light from the bottom side of the microfluidic cavity. The transmission peak at 908.76 nm has a FWHM of  $\sim 1.0$  nm, corresponding to a cavity finesse of 30. Further improvement of the measured cavity finesse is expected by exciting the cavity modes with a highly collimated tunable laser source.

Uniform clamping forces and a smooth bonding interface are required to assure the parallelism between the superstrate and the substrate. In this paper, the parallelism between the top and bottom cavity mirrors after the bonding process was determined from the variation in the absolute cavity length as a function of

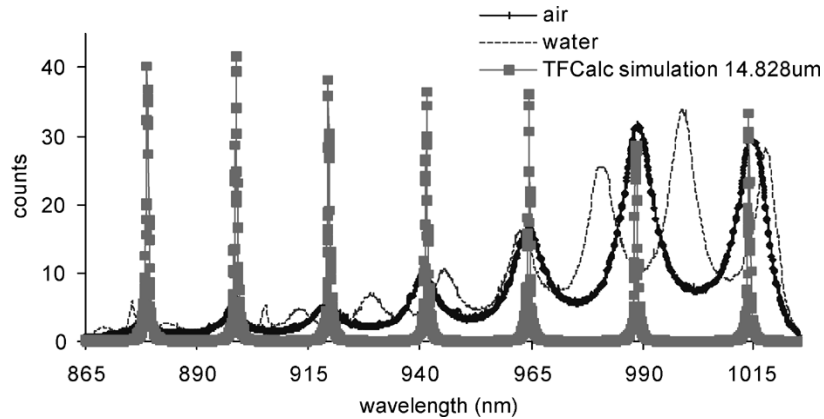


Fig. 5. Transmission spectra of a bonded microfluidic cavity filled with water and air, respectively, flood exposed by a broadband microscope white light. Also shown is a TFCalc simulation of the transmission spectra of the microfluidic Fabry–Pérot cavity after the thermocompressive bonding.

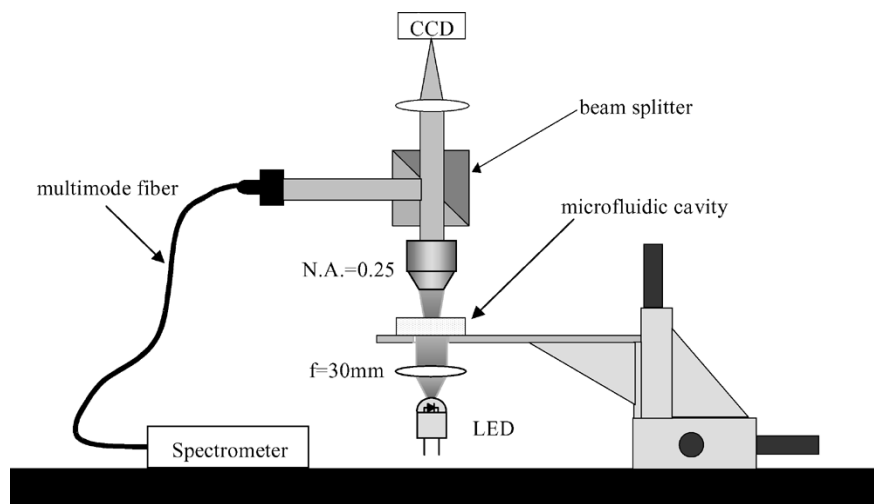


Fig. 6. Customized microscope system used to measure the optical spectra of the microfluidic Fabry–Pérot cavity.

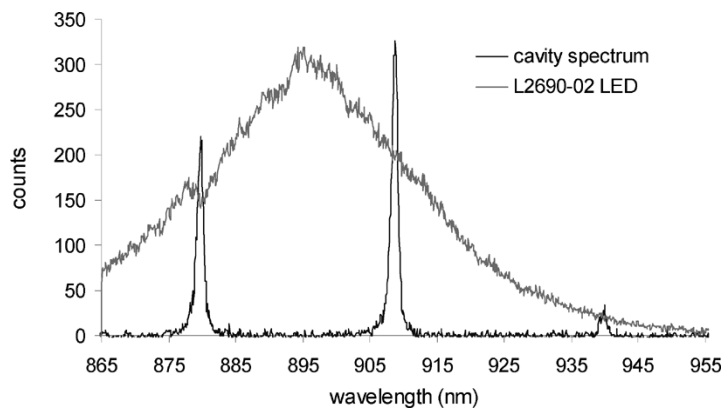


Fig. 7. Microfluidic FP cavity transmission spectrum illuminated with a well-collimated LED biased with a 100-mA current source. The spectrometer integration time was reduced by a factor of 30 for the LED spectrum in order to match with the intensity level of the microfluidic cavity spectrum.

position along the microfluidic channel. Fig. 8 shows the transmission spectra taken at seven different positions in a  $200\ \mu\text{m}$  wide,  $\sim 25\ \mu\text{m}$  deep microfluidic cavity filled with water. The transmitted light is collected from a circular spot of approximately  $10\ \mu\text{m}$  in diameter by adjusting the focus of the microscope system shown in Fig. 6. The absolute cavity length at each position can be calculated using  $L_{\text{cavity}} = c/(2 \cdot n \cdot \Delta\nu)$ , where  $\Delta\nu$  is the frequency difference of two neighboring longitudinal

modes of the Fabry–Pérot cavity,  $c$  is the speed of light in air, and  $n = 1.33$  is the refractive index of the water inside the microfluidic cavity. The deeper microfluidic cavity and larger refractive index used in this experiment allows many longitudinal modes in the transmission spectra, which increases the accuracy of the cavity length measurement and thus the mirror tilt angle calculation. The rms value of  $\Delta\nu$  for each spectrum is extracted from the curve and listed in Table II along with the corre-

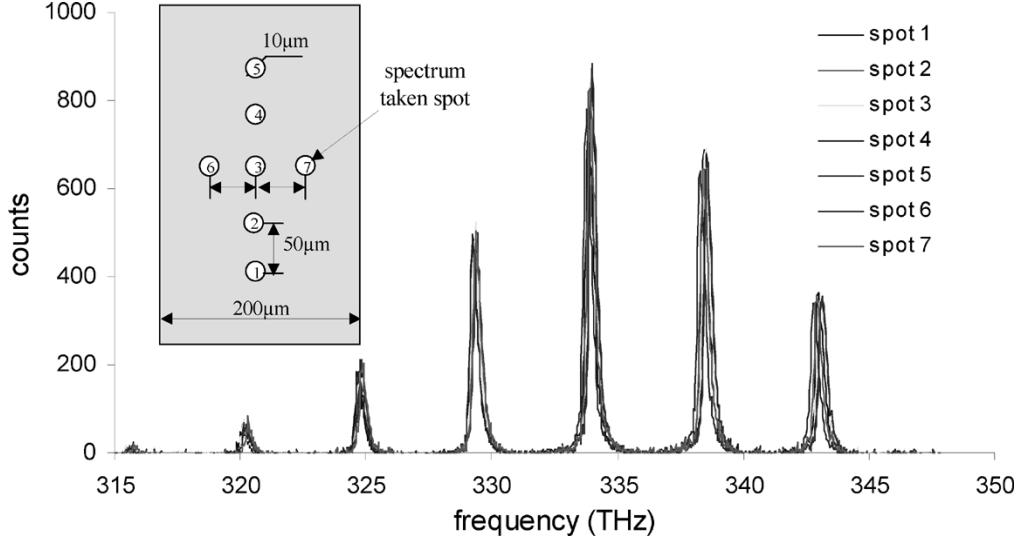


Fig. 8. Transmission spectra taken at seven different spots in a 200  $\mu\text{m}$  wide,  $\sim 25 \mu\text{m}$  deep microfluidic cavity filled with water after the thermocompressive wafer bonding. The inserted plot shows the spectra taken positions.

TABLE II  
FABRY-PÉROT CAVITY MIRROR PARALLELISM MEASUREMENT

Detection position	Peak 1 (THz)	Peak 2 (THz)	Peak 3 (THz)	Peak 4 (THz)	Peak 5 (THz)	Peak 6 (THz)	RMS $\Delta \nu$ (THz)	$L_{\text{cavity}}$ ( $\mu\text{m}$ )
1	320.119	324.815	329.334	333.875	338.598	342.959	4.570	24.679
2	320.085	324.633	329.243	333.875	338.432	342.959	4.575	24.652
3	320.113	324.721	329.337	333.905	338.501	343.065	4.590	24.569
4	320.198	324.753	329.37	333.97	338.535	343.175	4.596	24.542
5	320.113	324.78	329.337	333.972	338.535	343.100	4.598	24.531
6	320.113	324.721	329.337	333.875	338.467	343.065	4.590	24.569
7	320.113	324.753	329.234	333.875	338.261	343.012	4.582	24.616

sponding cavity length. The cavity mirror-tilting angle is calculated from  $\theta_{\text{tilt}} = \arctan(\Delta L_{\text{cavity}}/\Delta x)$ . Here  $\Delta L_{\text{cavity}}$  is the cavity length change from one position to the next position, and  $\Delta x$  is the distance between the two positions. The maximum tilt angles calculated from Table II are  $0.095^\circ$  and  $0.053^\circ$  in the direction transverse to and along the channel layout, respectively.

Departures of flat mirrors from perfect parallelism have been studied as a form of surface defect in FP cavities [12]. Mirror tilt induced cavity finesse can be calculated using a closed form formula derived by Sloggett,  $F_{\text{tilt}} = \sqrt{3}/(\pi\sigma_{\text{tilt}}) = \sqrt{3}/\pi(\phi_{\text{max}}/2)$ , where  $2\phi_{\text{max}}$  is the round-trip peak-to-peak phase variation across a circular aperture due to the nonparallelism of the flat interferometer plates. It can be calculated as  $\phi_{\text{max}} = (2\pi/\lambda)n(D/2)\tan(\Gamma_{\text{tilt}})$ , where  $D$  is the effective aperture size,  $n = 1.33$  is the refractive index of water inside the microfluidic cavity, and  $\Gamma_{\text{tilt}}$  is the mirror tilt angle. The allowed maximum finesse  $F_{\text{max}}$  of a tilted mirror FP cavity depends on  $F_{\text{tilt}}$  and the ideal finesse  $F_{\text{ideal}}$  according to  $F_{\text{max}} = (F_{\text{ideal}}^{-2} + F_{\text{tilt}}^{-2})^{-1/2}$ . The measured tilt angles of  $0.095^\circ$  and  $0.053^\circ$  correspond to cavity finesesses of 31.71 and 38.42, respectively, for an aperture size of 10  $\mu\text{m}$  in diameter and an ideal finesse of 43.28. For intracavity spectroscopy applications, exciting the microfluidic FP cavity using a smaller beam size is an effective way of reducing the mirror tilting effects [19]. Consideration of the combined effects of the mea-

sured surface roughness and mirror tilt provides a maximum calculated finesse of 30.99, which is in good agreement with the observed finesse of 30.

#### IV. CONCLUSION

In this paper, we reported a simple microfluidic channel fabrication process, which can be easily performed using simple fabrication equipment. The process described here allows the fabrication of microfluidic FP cavities without using additional spin-on glass layers or other types of UV sensitive glue to bond the glass substrates. It relies only on the metal films already deposited as an etch mask without further material deposition. Good reproducibility has been obtained using cleanroom procedures. Since the method does not require sophisticated polishing and cleaning steps, it should enable a wider range of researchers to fabricate customized microfluidic chips. Furthermore, it can be combined with highly reflective dielectric or metal thin film optical coatings in the etched channels to perform intracavity microscopy experiments in different wavelength ranges. The in-channel metal coating can also be used as electrodes to form microchips that are suitable for electrophoresis experiments. In general, the flexibility offered by this fabrication method should extend the applications of the conventional microfluidic FP cavities into chemical and biological spectroscopy experiments.

## ACKNOWLEDGMENT

The authors gratefully acknowledge the technical assistance from A. Al-Omari, G. W. Yuan, M. Raza, Y. Liu, J. A. Vickers, and Y. F. Lu.

## REFERENCES

- [1] K. E. Meissner, P. L. Gourley, T. M. Brennan, and B. E. Hammons, "Intracavity spectroscopy in vertical cavity surface-emitting lasers for micro-optical-mechanical systems," *Appl. Phys. Lett.*, vol. 69, no. 11, pp. 1517–1519, 1996.
- [2] P. L. Gourley, "Biocavity laser for high-speed cell and tumor biology," *J. Phys. D: Appl. Phys.*, vol. 36, pp. R228–R239, 2003.
- [3] B. Helbo, A. Kristensen, and A. Menon, "A micro-cavity fluidic dye laser," *J. Micromech. Microeng.*, vol. 13, pp. 307–311, 2003.
- [4] G. Minas, J. S. Martins, and J. H. Correia, "Highly selective optical detection in a lab-on-a-chip for biological fluids analysis," *Sens. Materials*, vol. 14, no. 2, pp. 7–89, 2002.
- [5] R. J. Jackman, T. M. Floyd, R. Ghodssi, M. A. Schmidt, and K. F. Jensen, "Microfluidic systems with on-line UV detection fabricated in photodefinable epoxy," *J. Micromech. Microeng.*, vol. 11, no. 3, pp. 263–269, 2001.
- [6] C. H. Lin, G. B. Lee, Y. H. Lin, and G. L. Chang, "A fast prototyping process for fabrication of microfluidic systems on soda-lime glass," *J. Micromech. Microeng.*, vol. 11, pp. 726–732, 2001.
- [7] I. Rodriguez, P. Spicar-Mihalic, C. L. Kuyper, G. S. Fiorini, and D. T. Chiu, "Rapid prototyping of glass microchannels," *Analytica Chimica Acta*, vol. 496, pp. 205–215, 2003.
- [8] S. C. Jacobson, R. Hergenroder, L. B. Koutny, R. J. Warmack, and J. M. Ramsey, "Effects of injection schemes and column geometry on the performance of microchip electrophoresis devices," *Anal. Chem.*, vol. 66, no. 7, pp. 1107–1113, 1994.
- [9] D. J. Harrison, A. Manz, Z. H. Fan, H. Lusi, and H. M. Widmer, "Capillary electrophoresis and sample injection systems integrated on a planar glass chip," *Anal. Chem.*, vol. 64, no. 17, pp. 1926–1932, 1992.
- [10] Z. H. Fan and D. J. Harrison, "Micromachining of capillary electrophoresis injectors and separators on glass chips and evaluation of flow at capillary intersections," *Anal. Chem.*, vol. 66, pp. 177–184, 1994.
- [11] R. A. Briones, L. O. Heflinger, and R. F. Wuerker, "Holographic microscopy," *Appl. Opt.*, vol. 17, p. 944, 1978.
- [12] G. J. Sloggett, "Fringe broadening in Fabry–Pérot interferometers," *Appl. Opt.*, vol. 23, no. 14, pp. 2427–2431, 1984.
- [13] C. S. Vikram and M. L. Billet, "Aberration limited resolution in Fraunhofer holography with collimated beams," *Opt. Laser Technol.*, vol. 21, p. 185, 1989.
- [14] R. Yokokawa, S. Takeuchi, and H. Fujita, "Ultra-smooth glass substrate for bioassay with motor proteins," *Analyst*, vol. 129, pp. 850–854, 2004.
- [15] M. Bu *et al.*, "A new masking technology for deep glass etching and its microfluidic application," *Sens. Actuators*, pp. 1–7, 2004.
- [16] [Online]. Available: <http://www.nasatech.com/Briefs/Oct02/NPO20076.html>
- [17] K. T. Turner, M. D. Thouless, and S. M. Spearing, "Mechanics of wafer bonding: Effect of clamping," *J. Appl. Phys.*, vol. 95, no. 1, pp. 349–355, 2004.
- [18] B. Helbo, A. Kristensen, and A. Menon, "A micro-cavity fluidic dye laser," *J. Micromech. Microeng.*, vol. 13, pp. 307–311, 2003.
- [19] P. L. Penna *et al.*, "Transmittivity profile of high finesse plane parallel Fabry–Pérot cavities illuminated by Gaussian beams," *Opt. Commun.*, vol. 162, pp. 262–279, 1999.



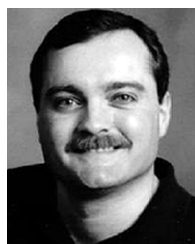
**Hua Shao** (S'04) received the B.S.E.E. and M.S. degrees in physics from Nanjing University of Science and Technology, Nanjing, China, in 1998 and 2001, respectively.

She is currently pursuing the Ph.D. degree in the Electrical and Computer Engineering Department, Colorado State University, Fort Collins. Her research interests include the design and fabrication of photonic biosensors, and numerical modeling of optical waveguides.



**Dhiraj Kumar** (S'03) received the B.E. degree in electronics and telecommunications engineering from Pt.Ravi Shankar Shukla University, Raipur, India, in 2002.

He is currently pursuing the M.S. degree in electrical engineering from Colorado State University, Fort Collins, where he is a graduate research assistant.



**Stewart A. Feld** (M'90) was born in Denver, CO, in 1966. He received the B.Sc. degree with honors in 1988, the M.Sc. degree in 1990, and the Ph.D. degree in electrical engineering in 1996, all from Colorado State University, Fort Collins.

From 1996 to 2000, he was with the Sensors Directorate of the Air Force Research Laboratory, WPAFB, pursuing research in the field of micro-cavity lasers. He has subsequently worked at several startup companies commercializing various types of vertical cavity laser technology. He is currently

with PowerSicel, Inc., Boulder, CO, where he is developing high-power high-frequency bipolar transistors using SiC-based materials.

Dr. Feld is a member of LEOS, SPIE, HKN, and Tau Beta Pi.



**Kevin L. Lear** (S'88–M'90) received the B.S.E.E. degree from the University of Colorado, Boulder, in 1984, and the M.S.E.E. and Ph.D.E.E. degrees from Stanford University, Stanford, CA, in 1985 and 1990, respectively.

He was a Senior Member of Technical Staff at Sandia National Laboratories from 1990 to 1997. In 1997, he became the Chief Scientific Officer at Micro Optical Devices, Inc., Albuquerque, NM, a small business commercializing VCSELs, subsequently acquired by Emcore Corporation. In 1999 he joined Colorado State University, Fort Collins, as the Rockwell Anderson Associate Professor of Electrical and Computer Engineering. His research is currently focused on photonic biosensors and components and systems for high speed optical communication.

Dr. Lear received an IEEE LEOS Distinguished Lecturer Award in 1996 for his work on VCSELs.